Nanoscale

ROYAL SOCIETY OF CHEMISTRY

COMMUNICATION

View Article Online
View Journal | View Issue

Cite this: *Nanoscale*, 2025, **17**, 19625

Received 12th May 2025,
Accepted 5th August 2025

DOI: 10.1039/d5nr01942g

rsc.li/nanoscale

Structural mechanisms of cellulose-based nanocomposites mimicking the structure of articular cartilage under uniaxial compression probed by *in situ* SAXS

Fanny Bosson,[a] Mohamed Karrouch,[a] Didier Blésès,[a] William Chèvremont,[b] Thomas Gibaud,[c] Laurent Michot,[d] Bruno Jean,[e] Vianney Delplace,[f] Nicolas Hengl[a] and Frédéric Pignon *[a]

A new method combining frontal ultrafiltration and ultrasound, followed by UV photocrosslinking enabled the fabrication of orthotropic CNC/PEGDA (poly(ethylene glycol) diacrylate) nanocomposites with the structure of articular cartilage. *In situ* SAXS compression/relaxation mechanical tests demonstrated this orthotropic organization as well as elastic behavior with a Young's modulus of 0.76 MPa, similar to articular cartilage.

Introduction

Human articular cartilage is a complex tissue with an overall thickness between 2 and 4 mm. It is composed of three depth-dependent zones: the superficial, intermediate, and deep zone, which account for 10–20%, 40–60%, and 30% of the total cartilage thickness, respectively.[1–3] Such an organization is referred to as orthotropic. In the three zones, collagen fibers are aligned in different orientations: parallel to the surface in the superficial zone, obliquely in the intermediate zone, and perpendicularly in the deep zone. These different orientations provide cartilage with both tensile strength and resistance to compressive forces. *In vivo*, articular cartilage can sustain significant compressive deformations of up to 30% without compromising its structural integrity.[4] Due to poor vascularization and limited proliferative capacity of chondrocytes, articular cartilage has a low ability to self-repair.[5] This makes cartilage repair a persistent challenge for both researchers and surgeons.[6]

Various tissue engineering approaches have been explored to reproduce this complex structure. For instance, hydrogels reinforced with cellulose nanocrystals (CNCs) have been studied to enhance the mechanical properties of scaffolds. However, such approaches are often limited due to insufficient interlayer adhesion.[7] Furthermore, they do not exhibit particle orientation within the matrix, which is needed for recreating the orthotropic structure of articular cartilage.[8] In contrast, techniques such as multilayer assembly can efficiently mimic cartilage structure and mechanical behavior. However, such strategies generally fail to reproduce the orthotropic organization in a single step.[9]

Cellulose, the most abundant polysaccharide in nature, plays a crucial role in providing plants with mechanical strength under stress.[10,11] CNCs, obtained through acid hydrolysis of cellulose, exhibit good mechanical properties with an axial elastic modulus of 110–220 GPa and a tensile strength of 7.5–7.7 GPa, making them ideal nanoparticles for reinforcing biomaterials.[12–14] In aqueous dispersions, CNCs are well distributed in space, thanks to repulsive electrostatic interactions between the CNCs, due to their charged surface. It has been shown the CNCs can self-organize into liquid crystal structures, further enhancing their versatility in biomedical applications.[10,15] CNCs have been widely explored for tissue engineering applications, including skin,[16] vascular,[17] cardiac,[18] liver,[19] bone,[20] and cartilage tissue engineering.[21]

The present study demonstrates the successful production of CNC/PEGDA nanocomposites that mimic the orthotropic structure of articular cartilage in a single step. This could be achieved by combining frontal ultrafiltration (FU) and ultrasound (US) for CNC orientation, and UV photocrosslinking for structure fixation. Through a detailed study of the binary phase diagram of CNC and PEGDA,[22] it was possible to start with conditions under which the liquid crystal behavior of CNCs is preserved in the presence of PEGDA. This in turn

[a]*Univ. Grenoble Alpes, CNRS, Grenoble INP (Institute of Engineering Univ. Grenoble Alpes), LRP, F-38000 Grenoble, France.*
E-mail: frederic.pignon@univ-grenoble-alpes.fr
[b]*ESRF, The European Synchrotron, F-38043 Grenoble, France*
[c]*Univ Lyon, ENS de Lyon, Univ Claude Bernard, CNRS, Laboratoire de Physique, F-69342 Lyon, France*
[d]*Sorbonne Université, CNRS, Physicochimie des Electrolytes et Nanosystèmes Interfaciaux, PHENIX, F-75005 Paris, France*
[e]*Univ. Grenoble Alpes, CNRS, CERMAV, F-38000 Grenoble, France*
[f]*Nantes Université, Oniris, CHU Nantes, INSERM, Regenerative Medicine and Skeleton, RMeS, UMR 1229, F-44000 Nantes, France*

enables their orientation by generating an acoustic streaming phenomenon induced by ultrasound.[7,23] Using such a strategy, CNCs could be aligned in different directions in the photocrosslinked nanocomposite, thus replicating the parallel and perpendicular orientations of collagen fibers in cartilage. This yielded a multilayer structure analogous to the superficial, intermediate, and deep zones of articular cartilage. Achieving distinct CNC orientations is crucial for obtaining mechanical properties akin to those of articular cartilage. Mechanical testing revealed a Young's modulus of 0.76 MPa, which is similar to that of articular cartilage.[24–26]

Results and discussion

Design of CNC/PEGDA nanocomposites with an orthotropic structure typical of articular cartilage

To prepare the initial CNC/PEGDA suspensions, CNCs (University of Maine, USA) at a stock concentration of 9.7 wt% were mixed with PEGDA (Sigma-Aldrich, France) with a molecular weight (MW) of 700 g mol^{-1} at a mass ratio (aqueous CNC suspension/pure PEGDA) of 80 : 20, thus resulting in a final CNC concentration of 7 wt%. The photoinitiator, Irgacure 2959 (Sigma-Aldrich, France), was added at a concentration of 0.6 wt% (Fig. 1a). The suspension was homogenized by magnetic stirring at room temperature. An FU–US filtration cell similar to that previously described[27–29] was used, with modifications to enable UV photocrosslinking (Fig. 1b). A 4 mm thick quartz glass was then added to the sides of the cell, which allowed UV light to pass through for *in situ* UV photocrosslinking during the FU–US processing. The overall design remained the same as previously used, featuring a parallelepiped filtration channel, 4 mm in width, 8 mm in depth, and 100 mm in length, along with a titanium vibrating blade, 3 mm wide and 100 mm long, that generates ultrasonic waves at 20 kHz. The CNC/PEGDA suspension was pumped into the channel, filling it completely, while an acoustic radiation force was applied vertically through the vibrating blade. The suspension was filtered in frontal mode on a 100 kDa PES membrane (Orélis Environnement, France) under a transmembrane pressure (ΔP) of 1.2 × 10^5 Pa, during which 1.2 W cm^{-2} of acoustic power (P_a) was applied. After a specific filtration time (t_f) of 1 hour, the feed channel was exposed to UV radiation (λ = 250–450 nm) for 120 seconds using a UV lamp (Omnicure S2000, France) (Fig. 1b). This UV photocrosslinking treatment was applied from one side of the filtration cell, allowing UV light to traverse from one side to the other thus generating UV photocrosslinking throughout the whole channel. To avoid the possible drying of the final composites that are hydrogels containing ≈73% water, photocrosslinked samples were stored in a Petri dish maintained in a humidity controlled environment (Fig. 1c).

Ex situ SAXS structural characterization

In order to characterize the structure of the photocrosslinked nanocomposites, *ex situ* SAXS measurements were performed at the TRUSAXS (Time Resolved Ultra Small Angle X-ray Scattering) Instrument of the European Synchrotron Radiation

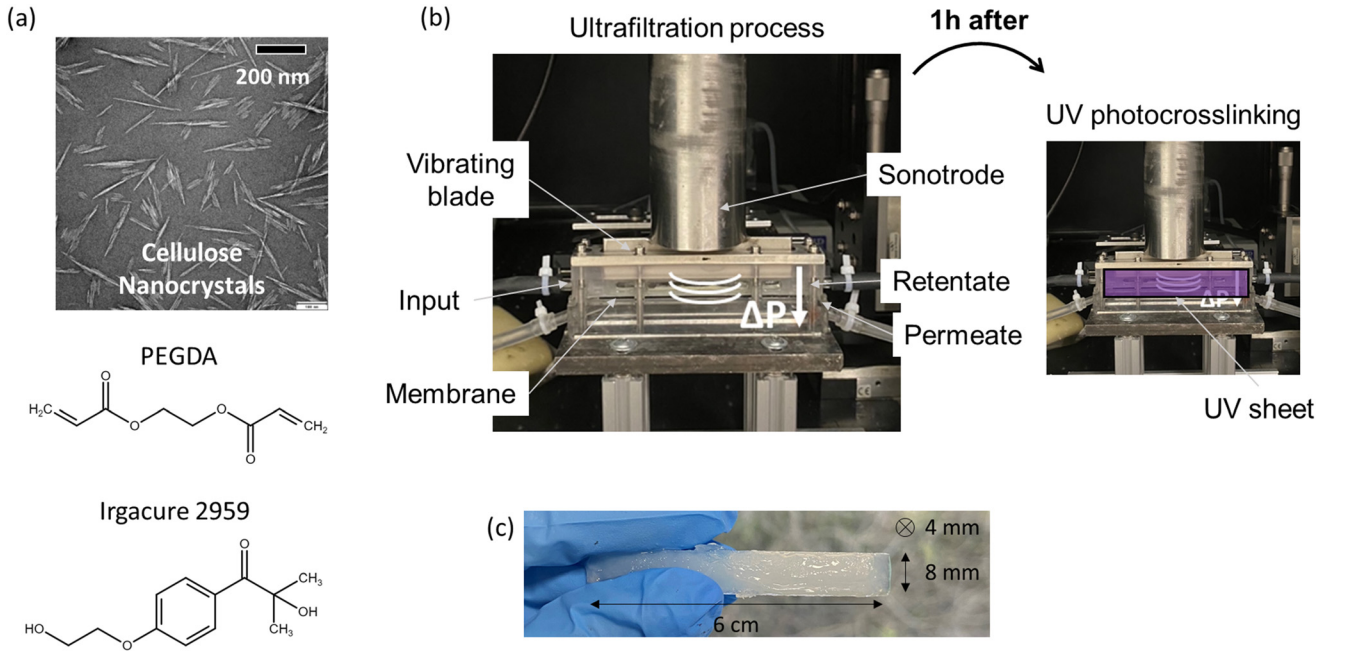

Fig. 1 CNC/PEGDA nanocomposite preparation. (a) Compounds used in the formulation of the nanocomposite: CNC, PEGDA, and the photoinitiator Irgacure 2959. (b) FU–US filtration setup. The CNC/PEGDA suspension is pumped into the channel. After 1 hour of filtration under a transmembrane pressure ΔP of 1.2 × 10^5 Pa and an acoustic power P_a of 1.2 W cm^{-2}, the UV blade is positioned on one side of the FU–US cell. This step enables the structure to be fixed by UV photocrosslinking. (c) Final composite sample in a humid state.

Facility (ESRF) in Grenoble, France (beamline ID02).[30] Experiments were conducted at room temperature, using a sample-to-detector distance of 1.5 m and a photon energy of 12.230 keV, which yielded a q-range extending from 0.02 to 2 nm^{-1}. The incident beam was approximately 30 μm high and 100 μm wide (FWHM), measured using a beam viewer.[30] The composite was aligned vertically to correspond with the applied transmembrane pressure, allowing the X-ray beam to pass parallel to the membrane surface. SAXS patterns were measured every 100 μm throughout the height of the photocrosslinked nanocomposite and recorded using a high-resolution hybrid pixel array detector (EIGER2-4M, Dectris). Normalized 2D patterns were provided by the standard processing pipeline of the instrument, after correction for the detector flatfield, solid angle subtended by the pixels and sample transmission. Further analysis involved azimuthal averaging of the normalized 2D patterns to generate intensity profiles, $I(q)$, where gaps between detector modules were patched using the SAXSutilities software.[31] Anisotropy was assessed using the MATLAB-based Small-Angle Scattering Evaluation Tool (SASET) software,[32] applying a model-free principal component analysis (PCA) method that produces values ranging from 0 for isotropic to 1 for a fully aligned pattern. This approach facilitated the calculation of anisotropy and the direction of maximum scattering (ψ_0) across q-ranges of 0.24–0.63 nm^{-1}. Using such an analysis, the impact of ultrafiltration and ultrasound on the orientation of CNCs in the nanocomposite can be precisely assessed.

The SAXS characterization of the CNC/PEGDA nanocomposite clearly reveals an orthotropic organization (Fig. 2a). During ultrafiltration of the CNC/PEGDA suspension, CNC particles accumulated near the membrane surface, as previously observed.[33–35] Such accumulation induced a preferential alignment of the CNCs characterized here by vertically oriented anisotropic SAXS patterns, indicating a horizontal orientation of CNCs close to the membrane.[36–38] In the upper region of the composite, where ultrasonic forces are predominant, the SAXS patterns also exhibited anisotropy but with a horizontal orientation, corresponding to a vertical alignment of CNCs. At the interface between these two zones, the balance between the ultrasonic waves and transmembrane pressure resulted in a random orientation of CNCs, evidenced by isotropic SAXS patterns, such as those shown in Fig. 2a, corresponding to a distance from the membrane of 4000 μm. A similar structural arrangement has previously been observed upon filtration of aqueous CNC suspensions.[27] However, maintaining the structure could not be achieved there. In contrast, in the present work, thanks to UV photocrosslinking, the structure is successfully preserved within a PEGDA hydrogel. The CNC alignment, dictated by the interplay of transmembrane pressure and ultrasonic forces, is locked, resulting in a stable orthotropic structure within the composite. This provides evidence that CNCs maintain their structural integrity and alignment in a solidified matrix, which is a key factor for developing materials with tailored mechanical properties.

In Fig. 2b, the blue curve representing the anisotropy parameter (PCA) of the sample is plotted as a function of distance

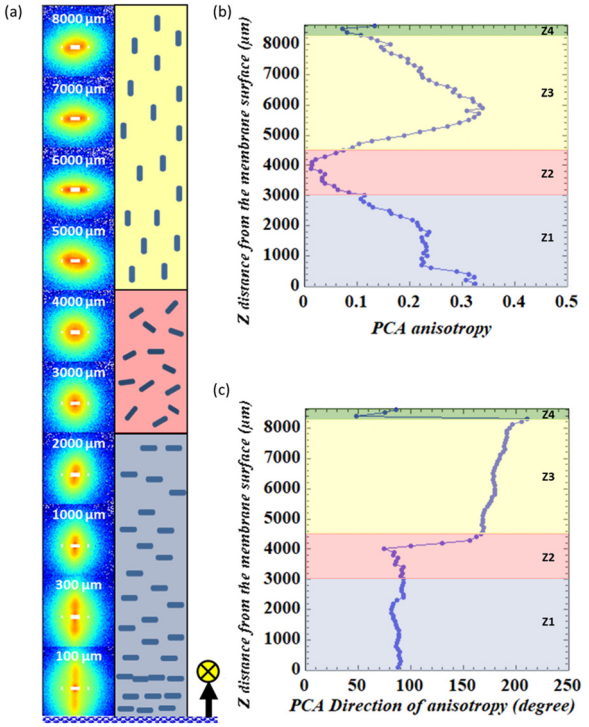

Fig. 2 Structural characterization, anisotropy and orientation analysis of the CNC/PEGDA nanocomposite. (a) Normalized 2D SAXS patterns of the CNC/PEGDA nanocomposite, recorded *ex situ* from the membrane surface to the vibrating blade with corresponding CNC orientation. (b) PCA anisotropy and (c) direction of anisotropy in degrees as a function of the distance Z from the membrane surface.

Z from the membrane surface. At short distances, the anisotropy remains relatively high, indicating a well-organized structure induced by the transmembrane pressure ($Z1$). This structure gradually fades until an isotropic state where the organization of CNCs becomes random at around 4000 μm. The isotropic region ($Z2$) corresponds to the transition zone where pressure and ultrasonic forces balance each other. Beyond this, the anisotropy increases again ($Z3$) until a maximum value of 0.3, before decreasing near the vibrating blade ($Z4$). This is linked to the acoustic streaming phenomenon that takes place in the upper part of the FU–US cell. The viscous attenuation of the acoustic wave in the CNC suspension creates an acoustic pressure gradient that induces vertical velocity fields in the filtration channel. Due to this physical phenomenon, the orientation of CNC nanoparticles is modified. The direction of anisotropy, shown in Fig. 2c (blue curve), remains around 90° up to 4000 μm, which indicates a horizontal alignment of the CNCs due to the transmembrane pressure near the membrane ($Z1$). Beyond this point, the orientation changes sharply to values between 170° and 210°, corresponding to a vertical alignment caused by an acoustic streaming force acting in the upper region of the composite ($Z3$).[39] The faster, smaller streaming rolls near the ultrasonic blade generate localized disturbances, explaining the final decrease in PCA and the last change in the direction of anisotropy ($Z4$).

Compression testing reveals the elastic behavior of the composite

The mechanical characterization of the nanocomposite was carried out using a compression testing machine developed at the "Laboratoire Rhéologie et Procédés" (Fig. 3). This machine allows precise control of the compression process and is equipped with a load cell able to measure forces up to 100 N with an accuracy of 0.1%. The samples, with dimensions of approximately 14 mm × 9 mm × 4.8 mm (width × height × thickness), were compressed to 30% of their original height at a speed of 0.1 mm s^{-1} at ambient temperature. The force was recorded over time along with the position of the upper jaw, enabling the generation of stress–strain curves to analyze the mechanical properties of the composites during compression. At the same time, SAXS characterization was extended to investigate the structural evolution of the composite during mechanical testing. Three *Z* scan measurements were performed at three key stages on the nanocomposites: before, during, and after releasing the compression.

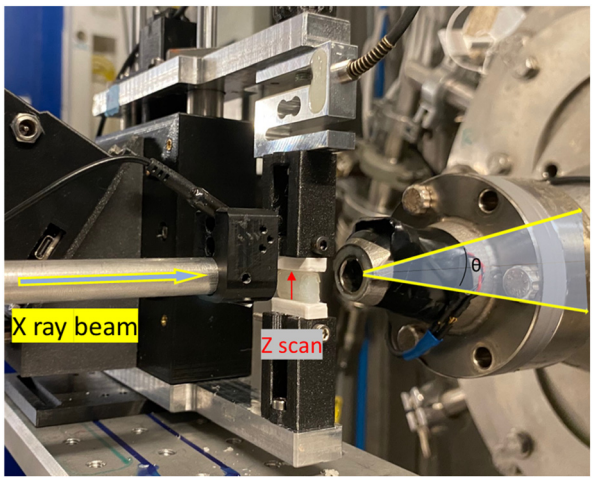

Fig. 3 Experimental set-up of the mechanical compression tests coupled with SAXS measurements.

The SAXS spectra obtained during compression (Fig. 4a) revealed that the orthotropic structure of the composite remains intact, as the three above-mentioned layers can be observed before, during, and after the mechanical compression test. Assuming that anisotropy parameters < 0.1 correspond to an isotropic organization, it is possible to calculate the thickness of the different layers (Fig. 4b). It appears that compression mainly affects the upper two layers (both isotropic and vertically oriented), whereas the horizontally oriented lower layer does not display significant evolution. This is confirmed by the evolution of the anisotropy para-

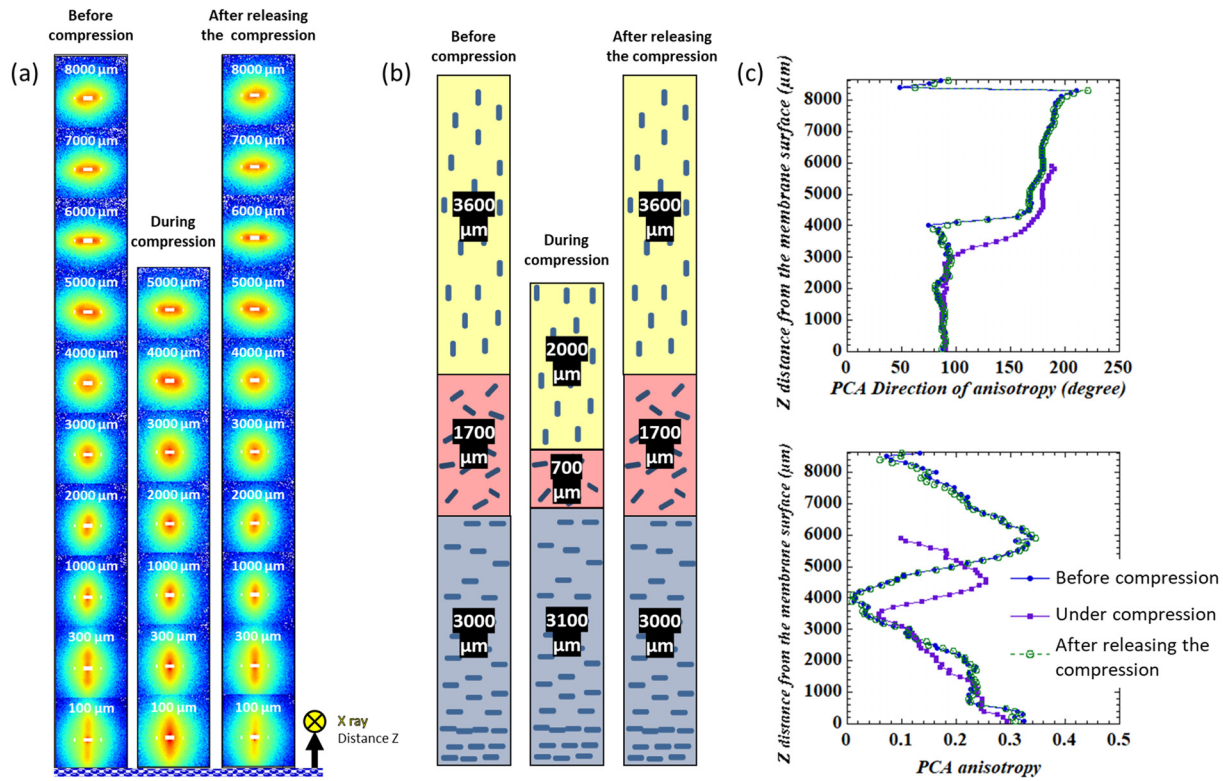

Fig. 4 SAXS results before, during, and after releasing the compression (ε = 30%). (a) Normalized 2D SAXS patterns of the CNC/PEGDA nanocomposite before, during, and after releasing the compression, recorded *ex situ* from the membrane surface to the vibrating blade. (b) Thickness of each layer before, during and after releasing the compression, with the corresponding CNC orientation. (c) PCA anisotropy and direction of anisotropy as a function of distance *Z* from the membrane surface before, during, and after releasing the compression.

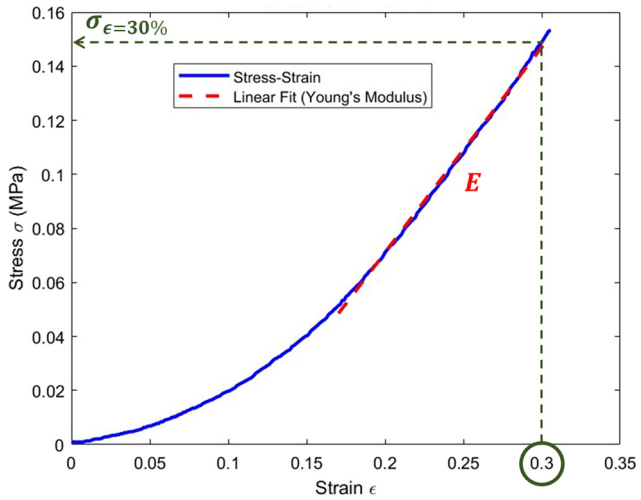

Fig. 5 Stress–strain curve of the CNC/PEGDA nanocomposite under compression (ε = 30%) with a Young's modulus of 0.76 MPa, calculated from the slope of the curve, and $\sigma_{\varepsilon=30\%}$ = 0.15 MPa.

meter, as a function of the normalized distance Z from the membrane surface, during compression (Fig. 4c), which shows that the bottom layer is only marginally affected. This observation can be linked to the fact that in the design of the compression set-up, only the upper grip is mobile. After releasing the compression, as shown by the green curve in Fig. 4c, the final structure exactly matches its pre-compression state, which further confirms the material's elastic behavior and the preservation of its overall structure. For clarity, the curves were also plotted as a function of the normalized distance Z from the membrane surface, confirming that deformation occurs mainly in the upper part of the composite (Fig. S1).

The stress–strain curve (Fig. 5) was used to calculate the Young's modulus of the composite. These mechanical compression tests were reproduced in the laboratory to assess the repeatability of the measurements (Fig. S2). The fully reversible nature of the stress–strain response indicates a hyperelastic behavior, which is characteristic of biological soft tissues such as cartilage. Hyperelastic materials can undergo large deformations and still return to their original shape without permanent damage, which is essential for tissues subjected to repetitive mechanical loading. The obtained value (0.76 ± 0.22 MPa) is similar to the Young's modulus of articular cartilage (~0.3–1.5 MPa (ref. 24–26)), further highlighting the potential of these nanocomposites for cartilage tissue engineering applications. Indeed, the observed match in mechanical properties suggests that these nanocomposites could be used as effective scaffolds for cartilage regeneration. The consistency of the structure before and after releasing the compression, combined with elastic recovery, further confirms the material's suitability for biomedical use.

Conclusions

In conclusion, thanks to the use of an original processing method combining frontal ultrafiltration, ultrasound, and UV photocrosslinking, we have been able to design novel CNC-PEGDA nanocomposites exhibiting a well-defined orthotropic structure reminiscent of that observed in articular cartilage. The obtained structure was accurately analyzed by synchrotron-based SAXS, taking full advantage of the small beam size available in such facilities. The latter were coupled with mechanical compression tests to correlate the change of the structural organization of the nanocomposite with the applied strength forces. The Young's modulus of the developed materials is close to that of the articular cartilage and SAXS studies carried out *in situ* during mechanical compression–decompression tests, confirming the elastic nature of the orthotropic composites. CNC/PEGDA nanocomposites thus represent a good model for studying the relationship between mechanical and structural properties in orthotropic structures. Furthermore, these materials could certainly be further optimized both in terms of mechanical properties and functionality by incorporating additional cartilage constituents, such as collagen. This could in turn allow the design of nanocomposites mimicking native cartilage that could be used for tissue engineering applications. However, future developments must address key challenges such as the scalability of the fabrication process and the effective integration of living cells within the composite matrix. These aspects open exciting opportunities for translating these bioinspired materials into clinically relevant tissue engineering solutions.

Author contributions

Fanny Bosson: writing – original, writing – reviewing and editing, formal analysis, and investigation; Mohamed Karrouch: technical design and investigation; Didier Blésès: technical design and investigation; William Chèvremont: investigation and writing – reviewing and editing; Thomas Gibaud: investigation and writing – reviewing and editing; Laurent Michot: investigation and writing – reviewing and editing; Bruno Jean: investigation and writing – reviewing and editing; Vianney Delplace: investigation, formal analysis, and writing – reviewing and editing; Nicolas Hengl: investigation, formal analysis, and writing – reviewing and editing; and Frédéric Pignon: conceptualization, methodology, draft preparation, writing – reviewing and editing, investigation, and formal analysis.

Conflicts of interest

There are no conflicts to declare.

Data availability

Data are available at **https://doi.esrf.fr/10.15151/ESRF-ES-1844907870**.

In SI, fig. S1 related to fig. 4, shows PCA anisotropy and direction of anisotropy as a function of the normalized distance Z from the membrane surface before, during, and after compression of a composite sample. Fig. S2 shows 5 successive

compression tests on the same orthotropic CNC/PEGDA composite allowing to asses the fully reversible nature of the stress-strain response and indicates a hyperelastic behavior. See DOI: https://doi.org/10.1039/d5nr01942g.

Acknowledgements

We would like to thank Theyencheri Narayanan (ESRF, Grenoble) for fruitful discussions and for his kind help in scattering experiments. We thank Frédéric Hugenell and Eric Faivre (Laboratoire Rhéologie et Procédés) for their technical assistance. ESRF is acknowledged for the provision of synchrotron beamtime (proposal SC-5605). The authors acknowledge the support of the French Agence Nationale de la Recherche (ANR), under grant ANR-20-CE43-0015 (ANISOFILM). LRP is part of LabEx Tec21 (Investissements d'Avenir – grant agreement #ANR-11-LABX-0030) of Institut Carnot PolyNat (Investissements d'Avenir – grant agreement #ANR-16-CARN-0025-01), and the Glyco@Alps programme (Investissements d'Avenir – grant agreement #ANR-15-IDEX-02).

References

1 L. T. Brody, *Phys. Ther. Sport*, 2015, **16**, 301–316.
2 C. Lesage, M. Lafont, P. Guihard, P. Weiss, J. Guicheux and V. Delplace, *Adv. Sci.*, 2022, **9**, 2200050.
3 A. J. Sophia Fox, A. Bedi and S. A. Rodeo, *Sports Health*, 2009, **1**, 461–468.
4 J. T. Bingham, R. Papannagari, S. K. Van de Velde, C. Gross, T. J. Gill, D. T. Felson, H. E. Rubash and G. Li, *Rheumatology*, 2008, **47**, 1622–1627.
5 S. L. Vega, M. Y. Kwon and J. A. Burdick, *Eur. Cells Mater.*, 2017, **33**, 59–75.
6 X. Yang, Z. Lu, H. Wu, W. Li, L. Zheng and J. Zhao, *Mater. Sci. Eng., C*, 2018, **83**, 195–201.
7 D. Liu, X. Dong, H. Liu, Y. Zhao and M. Qi, *J. Appl. Polym. Sci.*, 2021, **138**, 49856.
8 H. Golzar, Y. Wu, S. Ganguly and X. Tang, *Addit. Manuf.*, 2023, **73**, 103691.
9 S. Camarero-Espinosa, B. Rothen-Rutishauser, C. Weder and E. J. Foster, *Biomaterials*, 2016, **74**, 42–52.
10 C. Martin, phdthesis, Université Grenoble Alpes, 2015.
11 C. Schütz, J. R. Bruckner, C. Honorato-Rios, Z. Tosheva, M. Anyfantakis and J. P. F. Lagerwall, *Crystals*, 2020, **10**, 199.
12 R. M. A. Domingues, M. E. Gomes and R. L. Reis, *Biomacromolecules*, 2014, **15**, 2327–2346.
13 N. Pandi, S. H. Sonawane and K. Anand Kishore, *Ultrason. Sonochem.*, 2021, **70**, 105353.
14 B. Sun, M. Zhang, Q. Hou, R. Liu, T. Wu and C. Si, *Cellulose*, 2016, **23**, 439–450.
15 B. Frka-Petesic, B. Jean and L. Heux, *Cellulose*, 2023, **30**, 8311–8323.
16 L. Bacakova, J. Pajorova, M. Bacakova, A. Skogberg, P. Kallio, K. Kolarova and V. Svorcik, *Nanomaterials*, 2019, **9**, 164.
17 S. L. Arias, A. Shetty, J. Devorkin and J.-P. Allain, *Acta Biomater.*, 2018, **77**, 172–181.
18 N. Ma, D. Y. Cheung and J. T. Butcher, *J. Biomed. Mater. Res., Part A*, 2022, **110**, 76–91.
19 Y. Wu, Z. Y. Lin, A. C. Wenger, K. C. Tam and X. Tang, *Bioprinting*, 2018, **9**, 1–6.
20 A. Ali, S. Bano, S. Poojary, A. Chaudhary, D. Kumar and Y. S. Negi, *J. Biomater. Sci., Polym. Ed.*, 2022, **33**, 1–19.
21 D. Liu, H. Zhang, X. Dong, L. Sang and M. Qi, *Front. Bioeng. Biotechnol.*, 2022, **10**, 959409.
22 L. Metilli, S. Mandin, I. Chazapi, E. Paineau, W. Chèvremont, N. Hengl, F. Pignon and B. Jean, *J. Colloid Interface Sci.*, 2025, **685**, 476–486.
23 F. Bosson, M. Challamel, M. Karrouch, N. Hengl, H. Djeribi and F. Pignon, *Nanoscale*, 2025, **17**, 14381–14393.
24 J. P. A. Arokoski, M. M. Hyttinen, H. J. Helminen and J. S. Jurvelin, *J. Biomed. Mater. Res.*, 1999, **48**, 99–107.
25 M. T. Nieminen, J. Töyräs, J. Rieppo, J. M. Hakumäki, J. Silvennoinen, H. J. Helminen and J. S. Jurvelin, *Magn. Reson. Med.*, 2000, **43**, 676–681.
26 M. Laasanen, J. Töyräs, R. Korhonen, S. Saarakkala, M. Nieminen, J. Hirvonen and J. Jurvelin, *Biorheology*, 2003, **40**, 133–140.
27 F. Pignon, E. Guilbert, S. Mandin, N. Hengl, M. Karrouch, B. Jean, J.-L. Putaux, T. Gibaud, S. Manneville and T. Narayanan, *J. Colloid Interface Sci.*, 2024, **659**, 914–925.
28 Y. Jin, N. Hengl, S. Baup, F. Pignon, N. Gondrexon, M. Sztucki, A. Romdhane, A. Guillet and M. Aurousseau, *Carbohydr. Polym.*, 2015, **124**, 66–76.
29 Y. Jin, N. Hengl, S. Baup, F. Pignon, N. Gondrexon, A. Magnin, M. Sztucki, T. Narayanan, L. Michot and B. Cabane, *J. Membr. Sci.*, 2014, **453**, 624–635.
30 T. Narayanan, M. Sztucki, P. Van Vaerenbergh, J. Léonardon, J. Gorini, L. Claustre, F. Sever, J. Morse and P. Boesecke, *J. Appl. Crystallogr.*, 2018, **51**, 1511–1524.
31 M. Sztucki, *SAXSutilities2 (version 1.024)*, Zenodo, 2021.
32 M. Muthig, S. Prevost, R. Orglmeister and M. Gradzielski, *J. Appl. Crystallogr.*, 2013, **46**, 1187–1195.
33 S. Mandin, L. Metilli, M. Karrouch, C. Lancelon-Pin, J.-L. Putaux, W. Chèvremont, E. Paineau, N. Hengl, B. Jean and F. Pignon, *Carbohydr. Polym.*, 2024, **337**, 122162.
34 S. Mandin, L. Metilli, M. Karrouch, D. Blésès, C. Lancelon-Pin, P. Sailler, W. Chèvremont, E. Paineau, J.-L. Putaux, N. Hengl, B. Jean and F. Pignon, *Nanoscale*, 2024, **16**, 19100–19115.
35 C. Rey, N. Hengl, S. Baup, M. Karrouch, E. Gicquel, A. Dufresne, H. Djeridi, R. Dattani, Y. Jin and F. Pignon, *ACS Sustainable Chem. Eng.*, 2019, **7**, 10679–10689.
36 Q. Chen, P. Liu, F. Nan, L. Zhou and J. Zhang, *Biomacromolecules*, 2014, **15**, 4343–4350.
37 Z. Wang, Y. Yuan, J. Hu, J. Yang, F. Feng, Y. Yu, P. Liu, Y. Men and J. Zhang, *Carbohydr. Polym.*, 2020, **245**, 116459.
38 Z. Wang, N. Li, L. Zong and J. Zhang, *Curr. Opin. Solid State Mater. Sci.*, 2019, **23**, 142–148.
39 M. Wiklund, R. Green and M. Ohlin, *Lab Chip*, 2012, **12**, 2438–2451.